How to cite: *Angew. Chem. Int. Ed.* **2021**, *60*, 9553–9561
International Edition: doi.org/10.1002/anie.202017349
German Edition: doi.org/10.1002/ange.202017349

Controlled Release

Harnessing Hypoxia-Dependent Cyanine Photocages for In Vivo Precision Drug Release

*Yutao Zhang, Chenxu Yan, Qiaoqiao Zheng, Qian Jia, Zhongliang Wang, Ping Shi, and Zhiqian Guo**

Abstract: *Photocaging holds promise for the precise manipulation of biological events in space and time. However, current near-infrared (NIR) photocages are oxygen-dependent for their photolysis and lack of timely feedback regulation, which has proven to be the major bottleneck for targeted therapy. Herein, we present a hypoxia-dependent photo-activation mechanism of dialkylamine-substituted cyanine (Cy-NH) accompanied by emissive fragments generation, which was validated with retrosynthesis and spectral analysis. For the first time, we have realized the orthogonal manipulation of this hypoxia-dependent photocaging and dual-modal optical signals in living cells and tumor-bearing mice, making a breakthrough in the direct spatiotemporal control and in vivo feedback regulation. This unique photoactivation mechanism overcomes the limitation of hypoxia, which allows site-specific remote control for targeted therapy, and expands the phototrigger toolbox for on-demand drug release, especially in a physiological context with dual-mode optical imaging under hypoxia.*

Introduction

Light-mediated techniques with noninvasive nature and remote control have become a revolutionary tool in chemical biology.[1] Photocages that convert light into chemical energy to manipulate bioactive molecules allows finely spatiotemporal control.[2] Due to the unique tissue-transparent characteristic and low phototoxicity, near-infrared (NIR) photons have attracted immense attention for the design of such photocages.[3] However, the low energy of NIR-photons makes it difficult to directly achieve efficient bond cleavage in the context of living tissue.[4] Current NIR light-mediated cages mainly focus on the formation of singlet oxygen ($^1O_2$), via oxidizing of electron-rich olefins, resulting in bond-cleavage to restore bioactive molecules.[5] Here the major bottleneck of NIR photocages is that their photolysis reliance on O_2 consumption while hypoxia is ubiquitously aberrant at tumor.[6] Another challenge in caging design is difficult to simultaneously acquire in vivo feedback information for precise control in space and time. Hence, under hypoxia, it is an urgent conundrum to design such high-performance NIR photocages for specific targeting therapy.

Cyanine is a well-known NIR chromophore with high molar extinction coefficient and excellent biocompatibility.[7] However, its conjugated polymethine skeleton is inherently prone to light-dependent decomposition.[8] In this regard, converting the liability of cyanine bleaching for regulating photo-reactivity might be a novel and feasible strategy to engineer the NIR photocages. Regrettably, the reported cyanine-based photocages are all O_2-dependent consumption, which ascribes to the $^1O_2$-mediated cleavage of polyenes.[9] For instance, as a cage scaffold, heptamethine cyanines were all studied under sufficient O_2 supplement (Figure 1), and meanwhile their on-off fluorescence response mode made it difficult to achieve timely feedback, thereby limited their biological applicability. Aiming at these issues, the discovery of hypoxia-dependent photoactivation that reverses O_2 consumption could conquer the limitation of tumor hypoxia, thus perform precisely spatiotemporal light-mediated therapy.

Herein, we describe a unique cyanine-based photocage under hypoxia, in which its photolysis simultaneously produces dual-channel fluorescence and photoacoustic signals to permit finely manipulation in space and time. The hypoxia-dependent cage platform is firstly validated through retrosynthetic dialkylamine-substituted cyanine (Cy-NH), which undergoes retro-aldol, hydrolysis reaction to form a unique fragment under NIR light (> 650 nm) irradiation (Figure 1). Subsequently, the feasibility of cyanine-based photocages for targeted therapy is demonstrated via an elaborated P(Cy-N-CPT), which is sequence-activated by tumor acidic pH and light irradiation under hypoxia. In P(Cy-N-CPT), diblock copolymer containing ionizable tertiary amine renders ultrasensitive pH response for improved tumor-targeting, while the programmable Cy-NH photoactivation leads to dual-channel fluorescence and photoacoustic signals (PA).

This hypoxia-dependent P(Cy-N-CPT) is proven to be a highly successful one for site-specifically photorelease in living cells and mice. In fact, this uncaging strategy and dual-

[*] Y. Zhang, Dr. C. Yan, Prof. Dr. Z. Guo
Key Laboratory for Advanced Materials and Institute of Fine Chemicals, Feringa Nobel Prize Scientist Joint Research Center, Frontiers Science Center for Materiobiology and Dynamic Chemistry, School of Chemistry and Molecular Engineering, East China University of Science & Technology
Shanghai 200237 (China)
E-mail: guozq@ecust.edu.cn
Q. Zheng, Prof. Dr. P. Shi, Prof. Dr. Z. Guo
State Key Laboratory of Bioreactor Engineering, East China University of Science and Technology, Shanghai 200237 (P. R. China)
Q. Jia, Prof. Dr. Z. Wang
Engineering Research Center of Molecular-imaging and Neuro-imaging of Ministry of Education, School of Life Science and Technology, Xidian University, Xi'an, Shaanxi 710126 (China)
Supporting information and the ORCID identification number(s) for the author(s) of this article can be found under: https://doi.org/10.1002/anie.202017349.

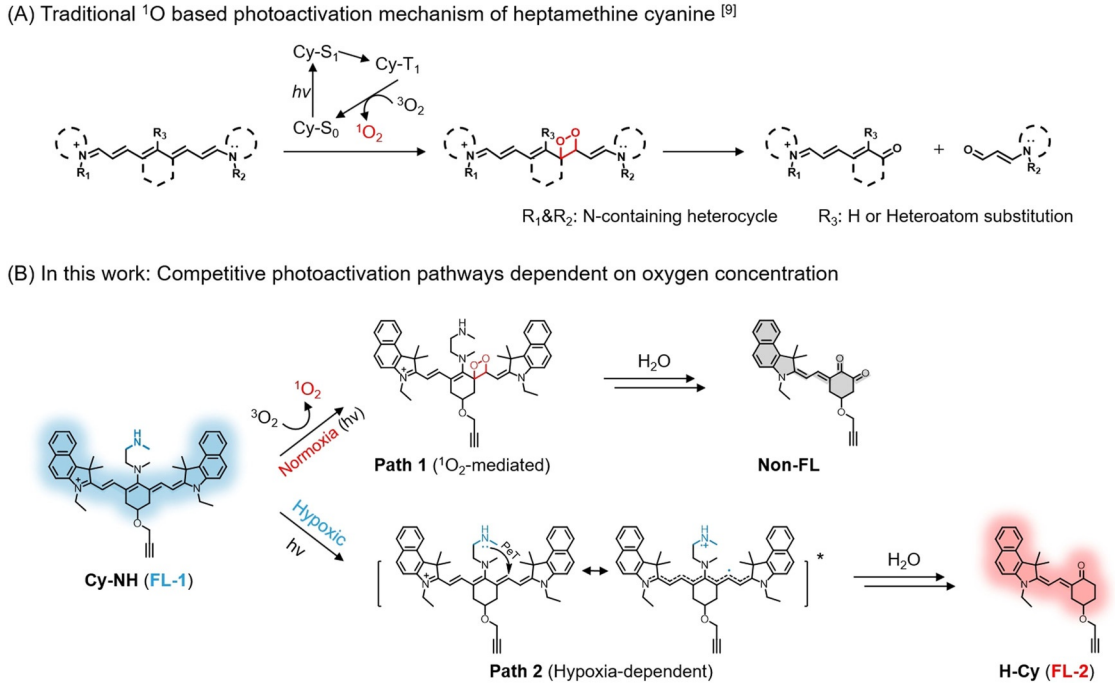

Figure 1. A) The reported photoactivation mechanism of cyanine is via $^1O_2$-mediated oxidative photocleavage of polyenes, and reliance on O_2-dependent consumption.[9] B) Competitive photoactivation pathways dependent on oxygen concentration. With the light irradiation under hypoxia, free radicals are possibly generated from Cy-NH, then result in the cleavage of Cy-NH, and concurrently produce dual-channel fluorescence output, thereby allowing precise NIR light-mediated therapy. Note: In Path 2, the photo-induced electron transfer (PeT) process occurs from the amino group to the methine chain of Cy-NH under hypoxia. The reference Cy-C without a secondary amine group further demonstrated that the amino group as electron donor plays the key role for the PeT process. This proposed radical-mediated photolysis is consistent with the reported cyanines.[10f] Finally, with the help of water as a reactant, the photolysis fragments H-Cy are obtained.

modal (dual-channel fluorescence and PA) output are optically orthogonal: the former allows for directly spatiotemporal control, and the latter permits real-time observation and in vivo feedback regulation. In detail, PA from the initial compact micelle of P(Cy-N-CPT) is utilized for in vivo tracking its biodistribution. When accumulated in acidic tumor, P(Cy-N-CPT) becomes into dissociated state with remarkable NIR fluorescence. Subsequently, under hypoxic tumor, NIR light-initiated photolysis leads to dual-channel fluorescence for monitoring drug release without blind spot. This discovery of hypoxia-dependent NIR photocage, combined with dual-modal optical signals, could open up a new route toward orthogonal remote control through time and dose of light, allowing site-specifically manipulation for in vivo targeting therapy.

Results and Discussion

Hypoxia-Dependent Photolysis of N-Substituted Heptamethine Cyanine

The defining feature of cyanines is an odd-carbon polyene linker with two nitrogen-containing heterocycles, but it is susceptible to photocleavage of the polyene chain. Indeed, under normoxia, the $^1O_2$- mediated photooxidation that derives from heptamethine cyanine photolysis are well studied. Clearly, this photooxidation of Cy-NH is O_2 consumption through the formation of dioxetane (Figure 1). However, we serendipitously observed and discovered that even under hypoxia, the photolysis of Cy-NH remains efficiency by a convenient 670 nm (±10 nm) laser source (10 mW cm^{-2}).

Seeking insights for this photolysis of heptamethine cyanine under hypoxia, we carried out a set of mechanism experiments (Figure 2). First of all, high-resolution electrospray ionization mass spectrometry (ESI-HRMS, Figure 2 A) was employed to reveal the photolysis fragmentation of Cy-NH under hypoxic condition by a convenient laser source. Notably, it was found that the peak at *m*/*z* 718.43 (corresponding to [Cy-NH$^{-\bullet}$ + H$^+$]) and 400.23 (corresponding to [H-Cy + H$^+$]) could identify the possible radical-based photoactivation. In detail, the peak at *m*/*z* 718.43 could be ascribed to the reaction of between Cy-NH$^{-\bullet}$ and H_3O^+ under NIR-light irradiation. It seems that the photo-induced electron transfer (PeT) process from an amino group to the Cy-NH triplet is very likely occurred,[10] then the exchange of "H" occurred through a polar process.[11] The elaborated Cy-C as a reference further confirmed the key role of an amine group for the PeT process (Figure S1), and thereby leading to the photolysis of Cy-NH under hypoxia. In the meantime, the peak at *m*/*z* 400.23 could be attributed to H-Cy as the photolysis fragmentation (Figure 2 A), which is clearly different from the $^1O_2$-mediated photolysis fragmentation at the peak of *m*/*z* 440.22 (Figure S2). All these results provided strong evidences that the hypoxia-dependent photolysis of

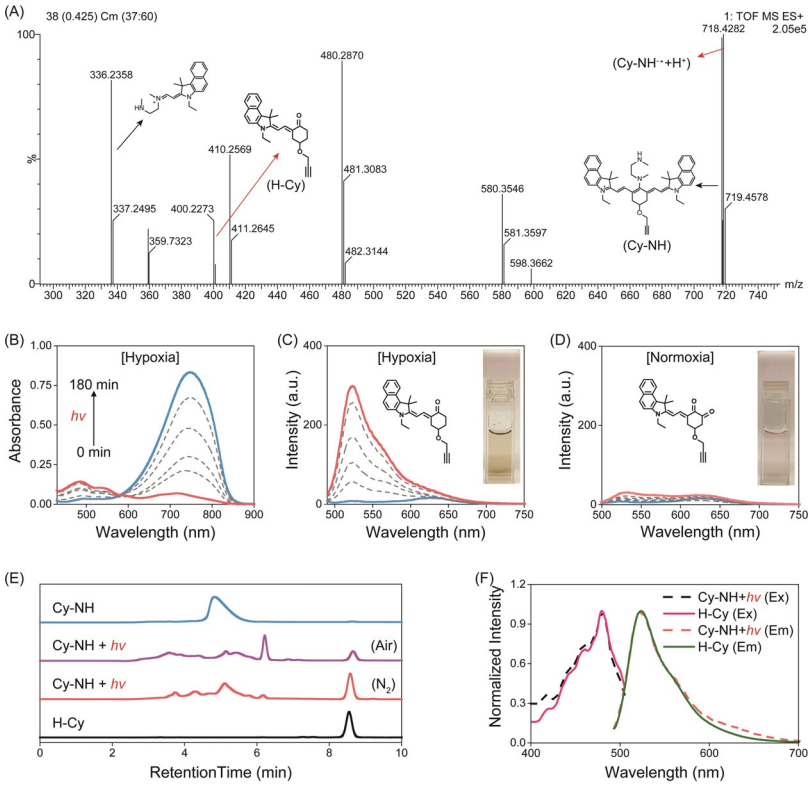

Figure 2. A) ESI-HRMS spectra of Cy-NH after NIR-light irradiation; spectral profiles of Cy-NH (10 μM) were carried out with a 670 nm (±10 nm) laser source (10 mW cm^{-2}) under B,C) hypoxia or D) normoxia in aqueous solution. E) HPLC traces of Cy-NH and H-Cy in air and N_2. F) Excitation and emission spectra of H-Cy and the NIR light-initiated fragments of Cy-NH under hypoxia.

Cy-NH occurs (Figure 1B and Figure S3–S4), that is, free radicals are generated from Cy-NH under NIR light irradiation, and thereby with the help of water as a reactant the photolysis fragments of H-Cy are obtained under hypoxia.

To further verify this proposed radical-mediated photoactivation under hypoxia, the retrosynthetic analysis of photolysis was carried out (Figure S5) and the synthetic route of H-Cy was elaborately depicted in Scheme S2. Luckily, we successfully obtained the synthesized H-Cy (Figure S6–S8). Subsequently, the spectra of H-Cy and the photolysis fragments of Cy-NH were analyzed. Specifically, the spectra of Cy-NH were recorded under normoxia or hypoxia with NIR-light irradiation, respectively. As shown in Figure 2B, under hypoxia, the NIR absorbance of Cy-NH at ca. 740 nm decreased in aqueous solution, while a concomitant new broad absorption peak appeared. Notably, the photolysis of Cy-NH under hypoxia showed a new strong emission with a tailed long-wavelength band (Figure 2C). In contrast, under normoxic with the same NIR light irradiation, there was observed similar absorption spectral change but non-fluorescence (Figure 2D and Figure S9). It was indicated that the photolysis fragmentation of Cy-NH under hypoxia is obviously distinct from that of under normoxia via well-defined $^1O_2$-mediated photoactivation.

To validate that H-Cy are completely the same as that of the hypoxic photolysis of Cy-NH, we employed high-performance liquid chromatography (HPLC) to trace the photolysis fragments of Cy-NH. Clearly, the retention time of the light-initiated fragment of Cy-NH under hypoxia was observed at 8.30 min, which is the same as that of H-Cy (Figure 2E and Figure S10–S13). Meanwhile, the absorption spectra mapped by the diode array detector are completely matched (Figure S12 and S13). It was convinced that the light-initiated fragment of Cy-NH under hypoxia is H-Cy. Furthermore, the excitation and emission spectra of the light-initiated fragment of Cy-NH under hypoxia are nearly identical with the H-Cy, suggesting that they are the same compound (Figure 2F, Figure S14, and Table S1–S2). Taken together, all these results provided solid evidences that under hypoxic conditions, the light-initiated photoactivated pathway of Cy-NH entails cleavage to generate H-Cy.

Hypoxia-Dependent Dual-Mode NIR Photocages

After reviewing this hypoxia-dependent photoactivation, we reasoned that Cy-NH could be a promising NIR light-initiated cage scaffold for optically orthogonal manipulation of fluorescence and photoacoustic (PA) signals. The sequence-activated photocage P(Cy-N-CPT) was elaborately designed (Figure 3), which is composed of an ionizable tertiary amine-containing diblock copolymer as ultra pH-sensitive unit to small pH differences between acidic tumor cells and blood, and is covalently bonded with a fluorescent Cy-NH cage for dual-modal optical signals.

We, therefore, performed light-initiated activation in aqueous solution to examine the feasibility of dual-modal optical signals. Firstly, the low critical micelle concentration of P(Cy-N-CPT) at 1.06 μg mL^{-1} indicated its initial formation of compact nanoparticles in aqueous solution (Figure 4A). The results of transmission electron microscopy (TEM) and dynamic light scattering (DLS) confirmed that P(Cy-N-CPT) forms compact and uniform nanoparticles with a hydrated particle size of about 60 nm (Figure 4B,C). Interestingly, when the hydrophobic block is protonated, the original compact micelle becomes disassemble (Figure 4D). Concurrently, the PA properties of P(Cy-N-CPT) towards concentration and assembled or disassembled micelles were investigated. Notably, the PA signals were plotted in a normalized phantom mold at various concentrations of P(Cy-N-CPT) (Figure 4E,F). The PA intensities at 720 nm indicated the superior PA properties of P(Cy-N-CPT) in the prosthesis (Figure 4G). Notably, there was a good linear relationship between the concentration and the mean PA signal (R^2 = 0.986 and R^2 = 0.987) (Figure S15). Thus, this intrinsic photoacoustic signal of P(Cy-N-CPT) could be utilized to real-time monitor its bio-distribution.

Next, we focused on whether P(Cy-N-CPT) could sense a subtle pH difference between the acidic endocytic organ-

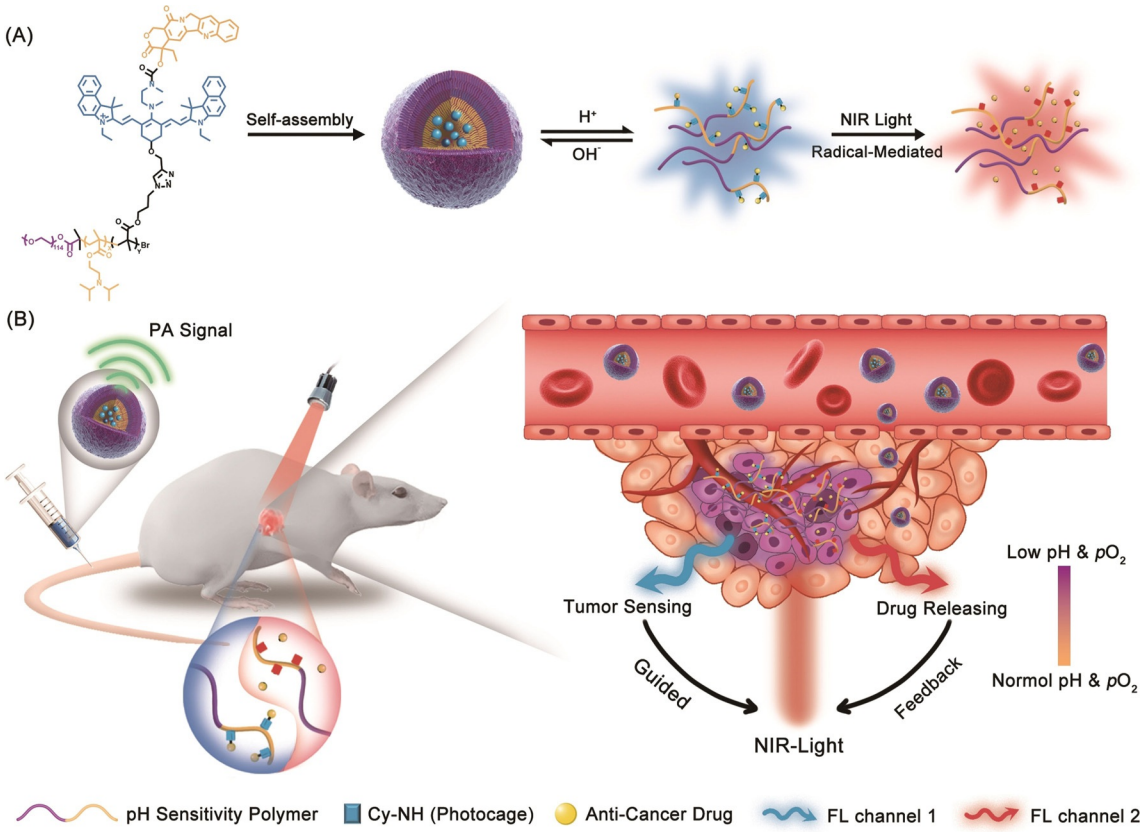

Figure 3. A) Schematic illustration of photocage with dual-modal PA and dual-channel fluorescence output. B) Schematic diagram of NIR light-initiated tumor-targeted precision drug release. At normal tissue with neutral pH, the photocage self-assembles as a compact micelle, with significant PA signal and non-fluorescence at 810 nm. At acidic tumor under hypoxia, the initial compact micelle dissociates with a dramatically increased fluorescence signal at 810 nm (FL channel 1). Subsequently, NIR light-initiated dual-channel fluorescence (a remarkable shift from 810 to 530 nm, FL channel 2) combined with PA signals occurs for tracking site-specifically activation of camptothecin (CPT) release.

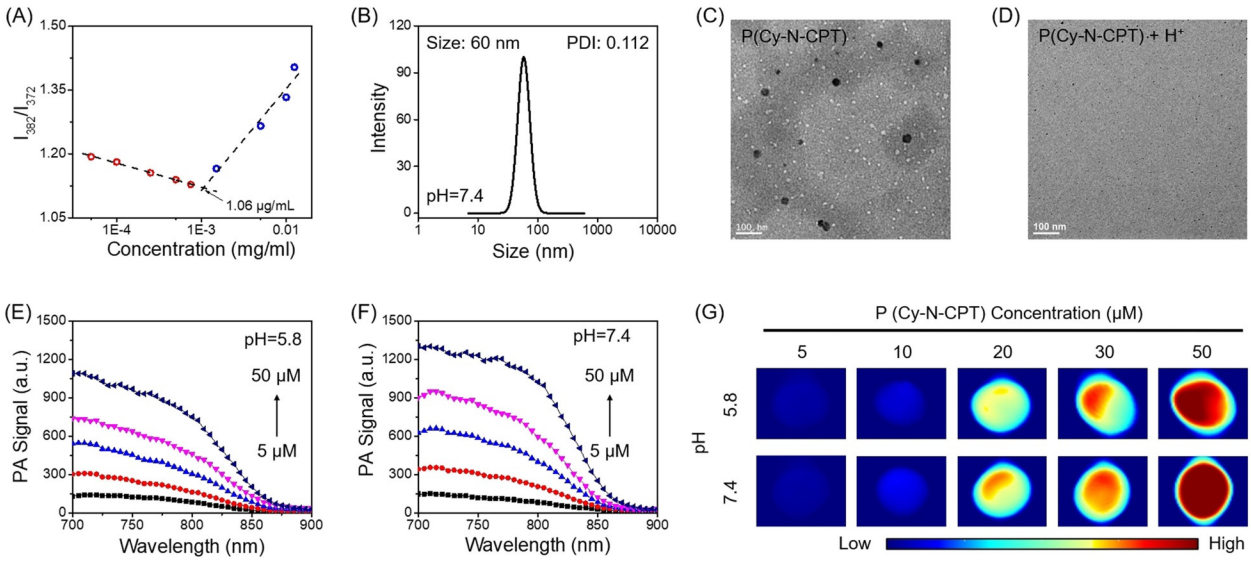

Figure 4. A) Critical micelle concentration (CMC) of P(Cy-N-CPT) at 37 °C. B) Size distribution of P(Cy-N-CPT). TEM images of P(Cy-N-CPT) in C) neutral or D) acid PBS solution (Scale bar = 100 nm). Photoacoustic spectra of P(Cy-N-CPT) in the normalized phantom mold at E) pH 5.8 and F) 7.4 PBS solution. G) Photoacoustic images at 720 nm of P(Cy-N-CPT) as a function of the concentration in the normalized phantom mold.

elles of cancer cells (5.0–6.0) and blood (7.4). As shown in Figure 5A, P(Cy-N-CPT) displayed a sharp pH transition ($pK_a = 6.0$, $\Delta pH_{ON/OFF} = 0.3$). At pH 7.4, P(Cy-N-CPT) formed compact self-assembled micelles, which completely

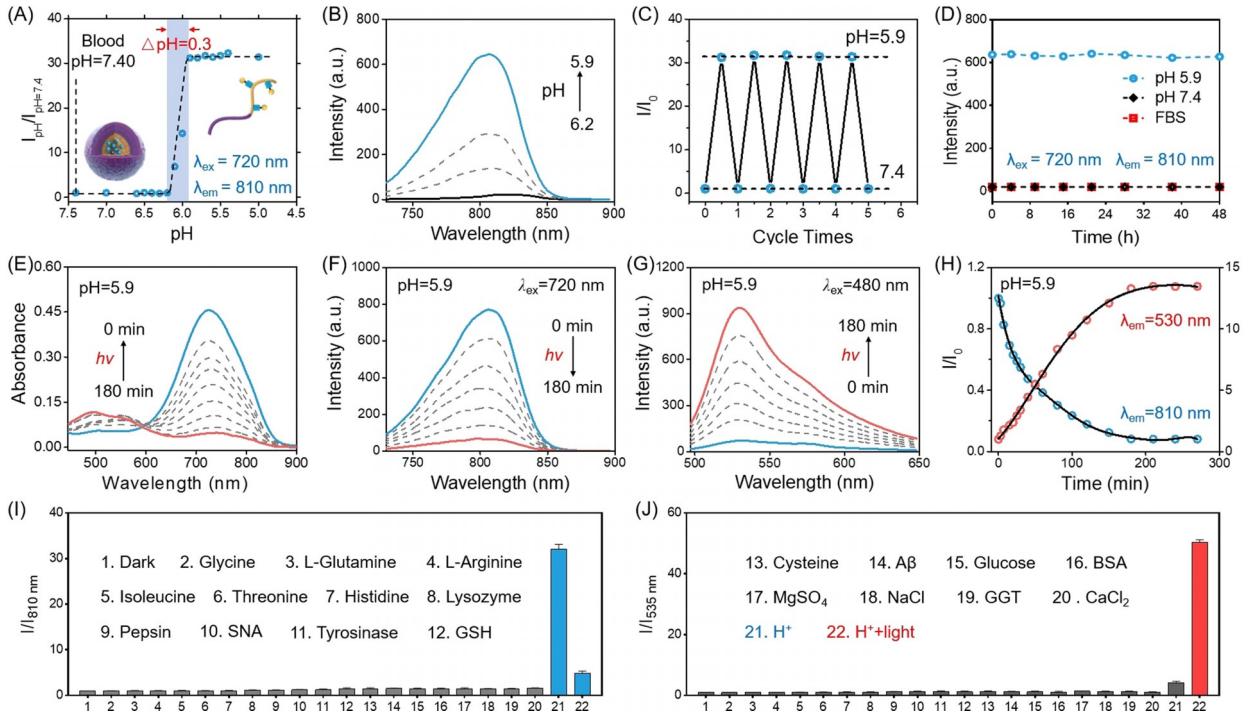

Figure 5. A) Fluorescence intensity as a function of pH alteration. P(Cy-N-CPT) keeps silent at high pH (7.4, 100 mM PBS buffer). At pH values below its pK_a transition (pH 6.0), P(Cy-N-CPT) is activated as a result of micelle dissociation. The pH response is extremely sharp ($\Delta pH_{ON/OFF} = 0.3$). B) Emission spectra ($\lambda_{ex} = 720$ nm) with various pH values (from 6.2 to 5.9). C) Reversibility study of P(Cy-N-CPT) toward pH at 37 °C. D) Stability study of P(Cy-N-CPT) in PBS and fetal bovine serum (FBS) over 48 h at 37 °C. Spectral characterization of P(Cy-N-CPT) at pH 5.9 in PBS buffer under hypoxia upon light irradiation (670 ± 10 nm, 20 mW cm^{-2}) E) absorption and emission spectra at F) $\lambda_{ex} = 720$ nm and G) $\lambda_{ex} = 480$ nm. H) Time-dependence of fluorescence changes at 810 and 530 nm. Fluorescence responses P(Cy-N-CPT) toward various amino acids, enzymes and serum potential markers in PBS buffer (pH 7.4) at 37 °C: I) $\lambda_{em} = 810$ nm and J) $\lambda_{em} = 535$ nm, including blank, glycine, L-glutamine, L-arginine, isoleucine, threonine, histidine, lysozyme, pepsin, SNA, tyrosinase, GSH, cysteine, Aβ, glucose, BSA, $MgSO_4$, NaCl, GGT, $CaCl_2$, H^+ (pH 5.9), H^+ + light (pH 5.9); each concentration is 50 μM.

silences the emission at 810 nm of Cy-N-CPT unit (Figure 5B). The phenomenon of the fluorescence "*OFF*" state resulting from the compact micelles could be further confirmed by the typical ACQ (aggregation-caused quenching) effect (Figure S16). In contrast, when the pH was decreased to 5.9, the original compact micelle was quickly disassembled, thereby leading to a dramatic light-up emission at 810 nm (Figure 5A,B). P(Cy-N-CPT) exhibited reversible pH-induced micelle transition with excellent sensitivity (Figure 5C), which is consistent with the TEM imaging results. Notably, the initial formed compact nanoparticles of P(Cy-N-CPT) kept stable for a long time in serum and neutral medium (Figure 5D), thereby protecting this photocage before photoactivation in heterogenous biological environment.

We subsequently performed light-initiated photolysis to validate dual-channel fluorescence output (a remarkable shift from 810 to 530 nm). As expected, upon NIR light irradiation with a convenient laser source, P(Cy-N-CPT) (at pH 5.9, below the transition) exhibited a remarkable shift change in absorption spectra, along with color change from blue to red in aqueous solution. As shown in Figure 5E, the absorption peak of P(Cy-N-CPT) at 720 nm was decreased and concomitantly a new broad absorption band was observed. Meanwhile, the emission spectra of P(Cy-N-CPT) underwent remarkable changes: the original NIR fluorescence at 810 nm ($\lambda_{ex} = 720$ nm) was gradually disappeared, and a new broad emission appeared and sharply increased (Figure 5F,G). It took about 180 min to reach the equilibrium of the NIR light-triggered photolysis (Figure 5H). Moreover, the interference analysis revealed that P(Cy-N-CPT) shows excellent selectivity over other biological analytes including amino acids, and proteins (Figure 5I,J). This dual-channel fluorescence output of P(Cy-N-CPT) allows for real-time monitoring of the NIR light-initiated release through time and dose of light without blind spot.

Clearly, the aforementioned light-initiated dual-mode optical signals (PA and dual-channel fluorescence output) could achieve precisely orthogonal manipulation in space and time for targeted therapy (Figure 3). In detail, the significant PA signal shows only slight changes during the micellar dissociation, thus tracking the delivery and biodistribution of P(Cy-N-CPT). Concurrently, the dramatic light-up fluorescence at 810 nm accurately guides for in vivo uncaging, and subsequently a remarkable shift from 810 to 600 nm (tailed emission) timely monitors this photolysis and camptothecin (CPT) release. Meanwhile, as feedback information, the NIR light-triggered fluorescence signal at 600 nm can regulate the external light dose (Figure 3B). The hypoxia-dependent photolysis and dual-modal optical output are orthogonal, enabling NIR light-initiated irradiation to precisely manipulate where, when and how the intact and active drugs are delivered.

Tracking NIR Light-Initiated In Vivo Behavior in Living Cells with Dual-Channel Fluorescence

We next investigated the feasibility of this light-initiated photocage for real-time tracking of cellular uptake and precise drug release for further biological application. A549 (Human adenocarcinoma cell) and HepG2 cells (Human hepatoma cell) were selected as cell models. Owing to the ultra-sensitive pH response, it is expected that P(Cy-N-CPT) keeps non-fluorescence in normal tissue, while specifically senses acidic tumor with light-up fluorescence. To gain insight into the light-mediated behavior, the intracellular photolysis of P(Cy-N-CPT) was intuitively observed by confocal laser microscopy. As shown in Figure 6, upon incubation P(Cy-N-CPT) with A549 and HepG2 cells, a ca. 20-fold enhancement of NIR emission at 810 nm was observed (Figure 6A,C and Figure S17). Notably, without washing process, the sharp enhancement fluorescence demonstrated that P(Cy-N-CPT) could accurately identify the acid endocytic organelles of tumor cells. Meanwhile, there was observed only one-channel NIR fluorescence without light irradiation, indicating that this photocage remains intact and non-specific cleavage during cellular uptake. In contrast, upon 670 nm light irradiation, a sharply decreased NIR fluorescence at 810 nm was found, and concomitantly a new enhanced emission at 535 nm was observed. Clearly, this dual-channel fluorescence output monitored the behaviors of the quick uptake and specific activation in a light-initiated manner (Figure 6B,D). These cell imaging results suggested that P(Cy-N-CPT) could be visualized to effectively sense the acidic endocytosis of tumor cells and then specific light-triggered release with dual-channel fluorescence changes.

To evaluate the light-dependent cytotoxicity, cell viability experiments of P(Cy-N-CPT) and its monomer Cy-N-CPT towards cancer cells (A549 and HepG2) were performed by MTT assay. In the absence of NIR light irradiation, P(Cy-N-CPT) and its monomer Cy-N-CPT exhibited negligible cytotoxic effects on cancer cells at the studied concentrations (0–10 μM), indicative of their good biocompatibility. After the external NIR light irradiation, P(Cy-N-CPT) showed significant cytotoxicity even at low concentrations (Figure 6E,F). Obviously, external light initiation is a key factor for the cytotoxicity of P(Cy-N-CPT) with the release of active CPT but no preference for the cell type. All these results clearly indicate that P(Cy-N-CPT) is solely light-dependent cytotoxicity in living cells. As a consequence, through the orthogonal time and dosage of light irradiation, the cellular behavior of P(Cy-N-CPT) becomes observable with the aid of dual-channel fluorescence, from effectively targeting tumor cells to specifically light-initiated drug release.

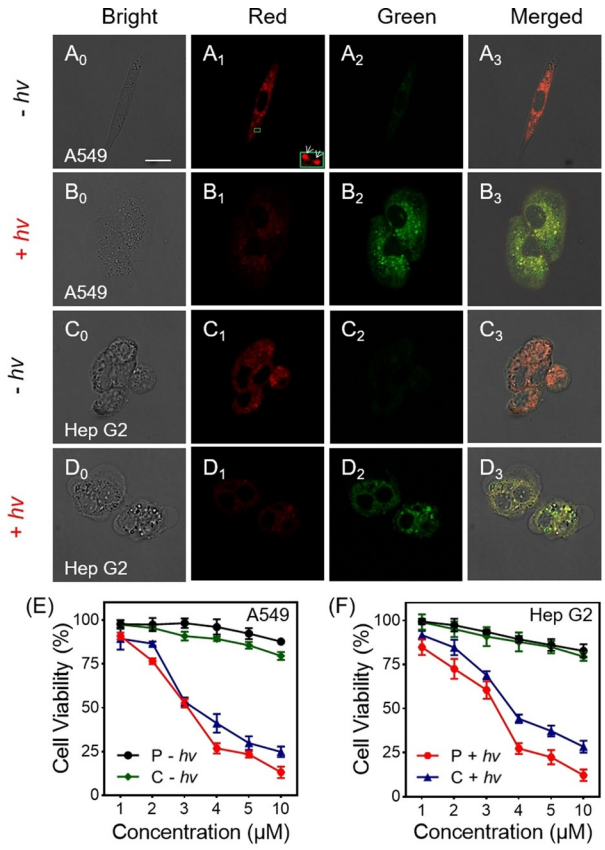

Figure 6. In vitro analysis of P(Cy-N-CPT) in A549 and HepG2 (cancer cells) with and without light irradiation (670 ± 10 nm, 20 mW cm^{-2}). Confocal microscopy images of cells incubated with P(Cy-N-CPT) (10 μM) for 2 h: A,C) without light irradiation (−); B,D) under light irradiation (+). The images were collected (A1, B1, C1 and D1) at the red channel (780 ± 20 nm, λ_{ex} = 633 nm) and (A2, B2, C2 and D2) at the green channel (535 ± 20 nm, λ_{ex} = 488 nm). E,F) Light-dependent cytotoxicity of P(Cy-N-CPT) in cell lines.

Mapping the Biodistribution via Photoacoustic Signals

Photoacoustic imaging is a powerful imaging modality capable of scalable spatial resolution and centimeter penetration.[12] When designing PA probe, it is essential for the chromophore featuring three key characteristics of NIR absorbance, large extinction coefficient and low fluorescence quantum.[13] In this cyanine-based photocage, P(Cy-N-CPT) initially forms compact micelles under natural physiological condition, thus leading to completely fluorescence quenching, while it still has a NIR absorbance with large extinction coefficient. Thus, these characteristics of P(Cy-N-CPT) make it as a perfect candidate to achieve significant photoacoustic signals, then for tracking in vivo biodistribution.

The high-resolution photoacoustic images of P(Cy-N-CPT) were recorded in a time-dependent method after intravenous injection with A549 xenograft tumor-bearing mice. As shown in Figure 7 (top), before intravenous injection, the tumor site exhibited initial weak PA signals at 720 nm on account of the intrinsic background signal. Whereas, at 24 h post-injection of P(Cy-N-CPT), the PA signal within the tumor showed a dramatic increment and reached up to a maximum, suggestive of the effective tumor-targeted accumulation (Figure 7 top and Figure S18). Furthermore, the 3D images of the tumor region provided solid evidence that P(Cy-N-CPT) passively permeated into the deep tumor (Figure 7, bottom). In contrast, other organs (such as spleen and intestine) displayed very weak photoacoustic signal. Obviously, the PA signals of P(Cy-N-CPT) could track it in

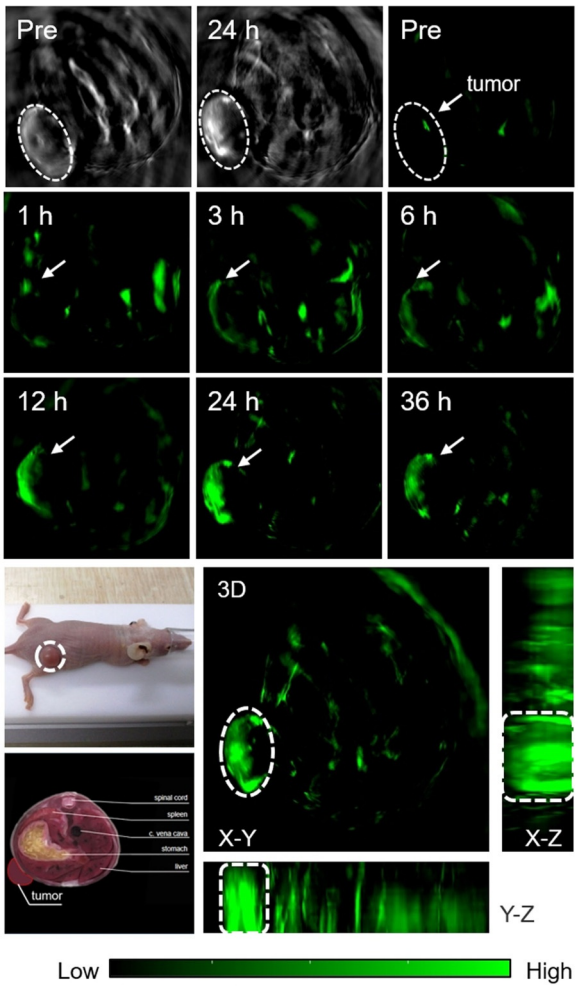

Figure 7. In vivo photoacoustic images of tumor tissue (white ellipse) at different times (top) and the 3D-images (bottom) at 24 h after the intravenous injection of P(Cy-N-CPT) (CPT-equivalent dose of 0.1 mg kg^{-1}, $\lambda_{ex} = 720$ nm). The white arrow indicates the tumor site. Note: In vivo mouse imaging experiments were repeated three times ($n = 3$).

vivo distribution and then visualize the location, shape, and size of solid tumors for accurately guiding NIR-light irradiation.

Harnessing Dual-Mode Optical Signals for Precision Drug Release in Space and Time

We next validate the orthogonal application of this hypoxia-dependent photocaging and dual-modal optical output, precisely in vivo manipulating where, when and how the intact and active drugs are delivered in living mice. In P(Cy-N-CPT), the ultra-sensitive pH-induced activation under acidic tumor and remarkable shift from dual-channel emission response made it perfect to real-time guide NIR-light stimulus and track the CPT release. In detail, the yellow-hot channel (emission at 810 nm) represents the disassemble of P(Cy-N-CPT) and the rainbow channel (emission at 600 nm) monitors light-triggered active drug release. After the intravenous injection of A549 xenograft tumor-bearing mice, a specific tumor-targeted accumulation of P(Cy-N-CPT) was visualized (Figure 8A,B). Consistently, the *ex vivo* imaging of the excised tumors further confirmed a high accumulation and then acidic activation with NIR light irradiation at tumor site (Figure 8C,D, and Figure S19, S20). Accordingly, there was much weaker fluorescence in the liver and almost no fluorescence in the other organs (heart, liver, spleen, lung, and kidney). The excellent tumor-targeting ability could be attributed to the synergistic effects of P(Cy-N-CPT): passive targeting from the EPR effect and activatable targeting (ultra-sensitive and reversible pH response). Notably, as a control of H^+ inhibition, $NaHCO_3$ solution was intratumorally injected before P(Cy-N-CPT) administration. Indeed, there was almost no fluorescence signal in the $NaHCO_3$ pre-treated group (Figure S21). All these results suggested that P(Cy-N-CPT) possesses striking characteristics of tumor-targeting, and then its self-assembly dissociation generates significant NIR signals, thereby allowing the guidance of light irradiation at the right site.

According to the in vivo imaging results without NIR light irradiation, the accumulation of fluorescence signals at the tumor site is time-dependent increased up to a maximum at 24 h (Figure 8A), which is consistent with the PAI results. Then, at the optimal time for in vivo photoactivation, we evaluated the light-initiated efficiency of P(Cy-N-CPT) at 24 h and the right position (timely fluorescence feedback on 810 nm). As shown in Figure 8E,F, under in vivo NIR-light (670 nm) irradiation, the emission signal at 810 nm decreased (yellow-hot channel), and concurrently new emission signal at 600 nm occurred (rainbow channel), confirming the desirable real-time tracking properties for site-specifically drug delivery at the tumor. Furthermore, the *ex vivo* studies also illustrated that the activated CPT was abundantly accumulated at the tumor and scarcely any appeared in other organs (Figure 8G,H). Both the in vivo and *ex vivo* imaging indicated that P(Cy-N-CPT) could be in vivo tracked via the activatable emission at 810 nm and thereby precisely guide the NIR light irradiation; then the concurrent emission at 600 nm is utilized for timely monitoring the drug release.

In this way, harnessing hypoxia-dependent photocaged cyanine, we take the dual-modality of fluorescence and photoacoustic imaging of P(Cy-N-CPT), tracking where, when and how the intact and active prodrugs are delivered in vivo. Specifically, photoacoustic signal has been serviced for real-time in vivo tracing where the intact prodrugs are located. At the same time, fluorescence signal (810 nm) from tumor tissue can be employed as the spatial guidance for the light irradiation, while according to timely feedback on another channel fluorescence signal (600 nm), the site-specifically initiation and dosage of light irradiation can finely regulate the activation and drug release.

Conclusion

In summary, we revealed a hypoxia-dependent cyanine-based photolysis mechanism, where P(Cy-N-CPT) leads to dual-mode optical signals under hypoxia, enabling precisely

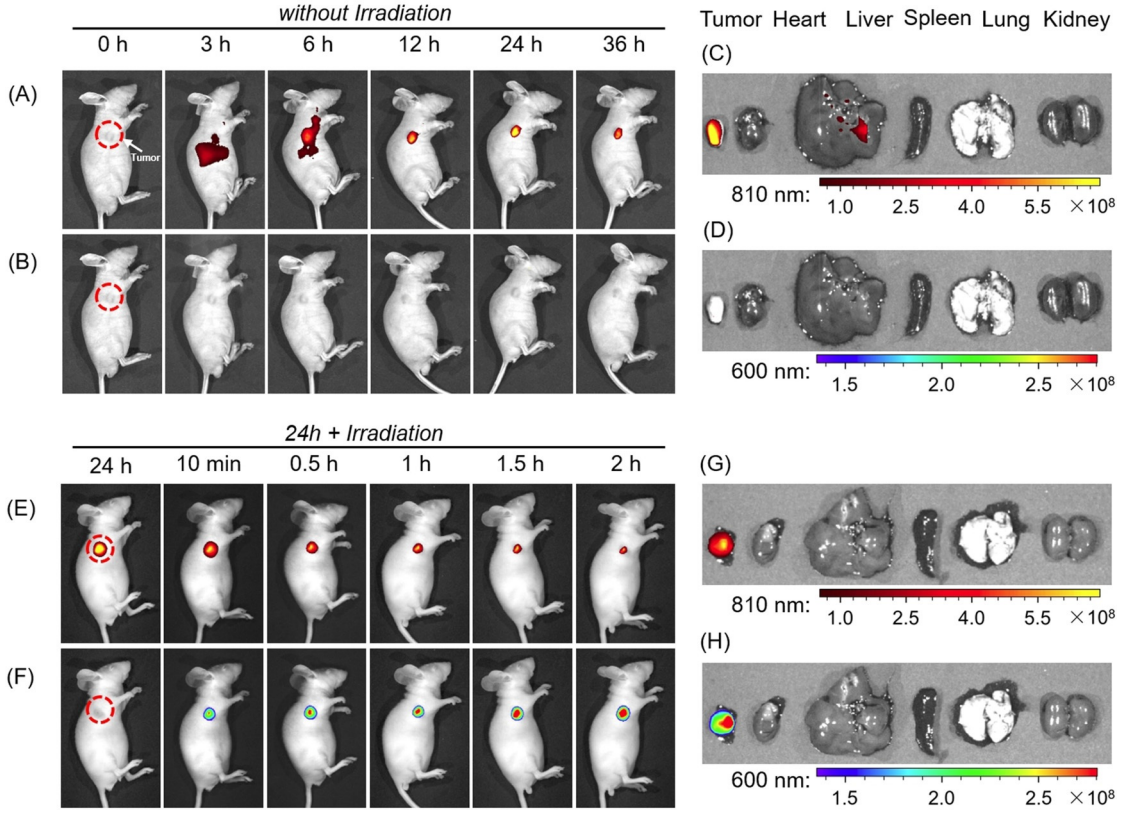

Figure 8. In vivo dual-channel NIR-fluorescence imaging of A549 xenograft tumor-bearing mice at various time (0, 3, 6, 9, 12, 24 h or under irradiation 10 min, 0.5 h, 1 h, 1.5 h and 2 h) after intravenous injection of P(Cy-N-CPT) E–H) with or A–D) without light irradiation (670 ± 10 nm, 200 mW cm^{-2}) administered at a CPT-equivalent dose of 0.1 mg kg^{-1}. The white arrow indicates the tumor site. Ex vivo NIR-fluorescence imaging of excised organs (heart, liver, spleen, lung, kidney and tumor) at 24 h or 36 h after the intravenous injection of P(Cy-N-CPT) (C, D, G and H). Note: In vivo mouse imaging experiments were repeated three times ($n = 3$).

remote control in space and time. We conducted a detailed retrosynthetic analysis and synthesized the corresponding fragments of Cy-NH through Vilsmeier–Haack, Aldol, and hydrolysis reaction, which confirmed our discovery of hypoxia-dependent photoactivation mechanism. This photocage P(Cy-N-CPT) was sequentially triggered by acidic pH and exogenous NIR light, thereby simultaneously producing dual-channel fluorescence and PA signals. Notably, unlike $^1O_2$-mediated photooxidation reliance on O_2-dependent consumption, our discovery of this cyanine photolysis conquers the limitation of tumor hypoxia, allowing remote control for targeted therapy. We have for the first time established finely orthogonal manipulation of hypoxia-dependent photocaging and dual-mode optical signals in living cells and tumor-bearing mice, thereby realizing spatiotemporal control and in vivo feedback regulation on light-mediated therapy. This hypoxia-dependent photolysis design strategy for dual-modality imaging would inspire the creation of a new generation of NIR photocages in a physiological context, thus greatly expanding the photo-triggered toolboxes for deep tissue penetration or phototherapy.

Acknowledgements

This work was supported by NSFC/China (21788102, 21878087 and 21908060), Shanghai Municipal Science and Technology Major Project (Grant 2018SHZDZX03), the Innovation Program of Shanghai Municipal Education Commission, the Shuguang Program (18SG27), the China Postdoctoral Science Foundation (2019M651417).

Conflict of interest

The authors declare no conflict of interest.

Keywords: cyanine · fluorescence imaging · hypoxia-dependent photolysis · near-infrared photocages · photoacoustic imaging

[1] a) H. B. Cheng, Y. Li, B. Z. Tang, J. Yoon, *Chem. Soc. Rev.* **2020**, *49*, 21–31; b) X. Li, J. F. Lovell, J. Yoon, X. Chen, *Nat. Rev. Clin. Oncol.* **2020**, *17*, 657–674; c) J. B. Grimm, B. P. English, H. Choi, A. K. Muthusamy, B. P. Mehl, P. Dong, T. A. Brown, J. Lippincott-Schwartz, Z. Liu, T. Lionnet, L. D. Lavis, *Nat. Methods* **2016**, *13*, 985–988; d) A. L. Vahrmeijer, M. Hutteman, J. R. van der Vorst, C. J. van de Velde, J. V. Frangioni, *Nat. Rev. Clin. Oncol.* **2013**, *10*, 507–518; e) L. Wu, A. C. Sedgwick, X. Sun,

S. D. Bull, X. P. He, T. D. James, *Acc. Chem. Res.* **2019**, *52*, 2582 – 2597; f) S. Long, Q. Qiao, L. Miao, Z. Xu, *Chin. Chem. Lett.* **2019**, *30*, 573 – 576.

[2] a) T. Wei, S. Lu, J. Sun, Z. Xu, X. Yang, F. Wang, Y. Ma, Y. S. Shi, X. Chen, *J. Am. Chem. Soc.* **2020**, *142*, 3806 – 3813; b) W. Zhang, F. Huo, Y. Yue, Y. Zhang, J. Chao, F. Cheng, C. Yin, *J. Am. Chem. Soc.* **2020**, *142*, 3262 – 3268; c) P. Klán, T. Solomek, C. G. Bochet, A. Blanc, R. Givens, M. Rubina, V. Popik, A. Kostikov, J. Wirz, *Chem. Rev.* **2013**, *113*, 119 – 191; d) M. Li, A. P. Dove, V. X. Truong, *Angew. Chem. Int. Ed.* **2020**, *59*, 2284 – 2288; *Angew. Chem.* **2020**, *132*, 2304 – 2308; e) Q. Lin, L. Yang, Z. Wang, Y. Hua, D. Zhang, B. Bao, C. Bao, X. Gong, L. Zhu, *Angew. Chem. Int. Ed.* **2018**, *57*, 3722 – 3726; *Angew. Chem.* **2018**, *130*, 3784 – 3788; f) N. Umeda, H. Takahashi, M. Kamiya, T. Ueno, T. Komatsu, T. Terai, K. Hanaoka, T. Nagano, Y. Urano, *ACS Chem. Biol.* **2014**, *9*, 2242 – 2246; g) Y. Chen, L. Li, W. Chen, H. Chen, J. Yin, *Chin. Chem. Lett.* **2019**, *30*, 1353 – 1360.

[3] a) Y. Zhu, H. Jia, G. Pan, N. W. Ulrich, Z. Chen, F. Wu, *J. Am. Chem. Soc.* **2018**, *140*, 4062 – 4070; b) K. Mitra, C. E. Lyons, M. C. T. Hartman, *Angew. Chem. Int. Ed.* **2018**, *57*, 10263 – 10267; *Angew. Chem.* **2018**, *130*, 10420 – 10424; c) E. D. Anderson, A. P. Gorka, M. J. Schnermann, *Nat. Commun.* **2016**, *7*, 13378; d) E. Palao, T. Slanina, L. Muchova, T. Solomek, L. Vitek, P. Klan, *J. Am. Chem. Soc.* **2016**, *138*, 126 – 133; e) T. A. Shell, J. R. Shell, Z. L. Rodgers, D. S. Lawrence, *Angew. Chem. Int. Ed.* **2014**, *53*, 875 – 878; *Angew. Chem.* **2014**, *126*, 894 – 897.

[4] a) J. M. Silva, E. Silva, R. L. Reis, *J. Controlled Release* **2019**, *298*, 154 – 176; b) T. Šolomek, J. Wirz, P. Klán, *Acc. Chem. Res.* **2015**, *48*, 3064 – 3072.

[5] a) C. G. Dariva, J. F. J. Coelho, A. C. Serra, *J. Controlled Release* **2019**, *294*, 337 – 354; b) P. Rajaputra, M. Bio, G. Nkepang, P. Thapa, S. Woo, Y. You, *Bioorg. Med. Chem.* **2016**, *24*, 1540 – 1549; c) P. Thapa, M. Li, M. Bio, P. Rajaputra, G. Nkepang, Y. Sun, S. Woo, Y. You, *J. Med. Chem.* **2016**, *59*, 3204 – 3214; d) F. Zhang, Q. Wu, H. Liu, *Wiley Interdiscip. Rev. Nanomed. Nanobiotechnol.* **2020**, *12*, 1643.

[6] a) X. Li, S. Yu, Y. Lee, T. Guo, N. Kwon, D. Lee, S. C. Yeom, Y. Cho, G. Kim, J. Huang, S. Choi, K. T. Nam, J. Yoon, *J. Am. Chem. Soc.* **2019**, *141*, 1366 – 1372; b) X. Zhao, S. Long, M. Li, J. Cao, Y. Li, L. Guo, W. Sun, J. Du, J. Fan, X. Peng, *J. Am. Chem. Soc.* **2020**, *142*, 1510 – 1517; c) H. Li, X. Li, W. Shi, Y. Xu, H. Ma, *Angew. Chem. Int. Ed.* **2018**, *57*, 12830 – 12834; *Angew. Chem.* **2018**, *130*, 13012 – 13016; d) S. Y. Lim, K. H. Hong, D. I. Kim, H. Kwon, H. J. Kim, *J. Am. Chem. Soc.* **2014**, *136*, 7018 – 7025; e) N. Narayanaswamy, S. Narra, R. R. Nair, D. K. Saini, P. Kondaiah, T. Govindaraju, *Chem. Sci.* **2016**, *7*, 2832 – 2841; f) J. V. Frangioni, *Curr. Opin. Chem. Biol.* **2003**, *7*, 626 – 634.

[7] a) X. Li, N. Kwon, T. Guo, Z. Liu, J. Yoon, *Angew. Chem. Int. Ed.* **2018**, *57*, 11522 – 11531; *Angew. Chem.* **2018**, *130*, 11694 – 11704; b) D. M. Gilkes, G. L. Semenza, D. Wirtz, *Nat. Rev. Cancer* **2014**, *14*, 430 – 439; c) M. S. Nakazawa, B. Keith, M. C. Simon, *Nat. Rev. Cancer* **2016**, *16*, 663 – 673; d) A. Sharma, J. F. Arambula, S. Koo, R. Kumar, H. Singh, J. L. Sessler, J. S. Kim, *Chem. Soc. Rev.* **2019**, *48*, 771 – 813.

[8] a) L. Jiao, Y. Liu, X. Zhang, G. Hong, J. Zheng, J. Cui, X. Peng, F. Song, *ACS Cent. Sci.* **2020**, *6*, 747 – 759; b) X. Chen, X. Peng, A. Cui, B. Wang, L. Wang, R. Zhang, *J. Photochem. Photobiol. A* **2006**, *181*, 79 – 85; c) D. H. Li, C. L. Schreiber, B. D. Smith, *Angew. Chem. Int. Ed.* **2020**, *59*, 12154 – 12161; *Angew. Chem.* **2020**, *132*, 12252 – 12259; d) R. R. Nani, J. A. Kelley, J. Ivanic, M. J. Schnermann, *Chem. Sci.* **2015**, *6*, 6556 – 6563; e) V. Rapozzi, L. Beverina, P. Salice, G. A. Pagani, M. Camerin, L. E. Xodo, *J. Med. Chem.* **2010**, *53*, 2188 – 2196; f) Z. Guo, Y. Ma, Y. Liu, C. Yan, P. Shi, H. Tian, W.-H. Zhu, *Sci. China Chem.* **2018**, *61*, 1293 – 1300.

[9] a) J. Peng, A. Samanta, X. Zeng, S. Han, L. Wang, D. Su, D. Loong, N. Kang, S. Park, A. H. All, W. Jiang, L. Yuan, X. Liu, Y. T. Chang, *Angew. Chem. Int. Ed.* **2017**, *56*, 4165 – 4169; *Angew. Chem.* **2017**, *129*, 4229 – 4233; b) A. P. Gorka, R. R. Nani, J. Zhu, S. Mackem, M. J. Schnermann, *J. Am. Chem. Soc.* **2014**, *136*, 14153 – 14159; c) A. P. Gorka, M. J. Schnermann, *Curr. Opin. Chem. Biol.* **2016**, *33*, 117 – 125; d) R. R. Nani, A. P. Gorka, T. Nagaya, T. Yamamoto, J. Ivanic, H. Kobayashi, M. J. Schnermann, *ACS Cent. Sci.* **2017**, *3*, 329 – 337; e) M. S. Baptista, J. Cadet, P. D. Mascio, A. A. Ghogare, A. Greer, M. R. Hamblin, C. Lorente, S. C. Nunez, M. S. Ribeiro, A. H. Thomas, M. Vignoni, T. M. Yoshimura, *Photochem. Photobiol.* **2017**, *93*, 912 – 919.

[10] a) M. Heilemann, E. Margeat, R. Kasper, M. Sauer, P. Tinnefeld, *J. Am. Chem. Soc.* **2005**, *127*, 3801 – 3806; b) G. T. Dempsey, M. Bates, W. E. Kowtoniuk, D. R. Liu, R. Y. Tsien, X. Zhuang, *J. Am. Chem. Soc.* **2009**, *131*, 18192 – 18193; c) A. P. Demchenko, *Methods Appl. Fluoresc.* **2020**, *8*, 022001; d) V. Glembockyte, G. Cosa, *J. Am. Chem. Soc.* **2017**, *139*, 13227 – 13233; e) P. Holzmeister, A. Gietl, P. Tinnefeld, *Angew. Chem. Int. Ed.* **2014**, *53*, 5685 – 5688; *Angew. Chem.* **2014**, *126*, 5792 – 5796; f) Y. Gidi, L. Payne, V. Glembockyte, M. S. Michie, M. J. Schnermann, G. Cosa, *J. Am. Chem. Soc.* **2020**, *142*, 12681 – 12689.

[11] a) H. Kasai, Z. Yamaizumi, M. Berger, J. Cadet, *J. Am. Chem. Soc.* **1992**, *114*, 9692 – 9694; b) J. Cadet, T. Douki, J.-L. Ravanat, *Acc. Chem. Res.* **2008**, *41*, 1075 – 1083.

[12] a) J. Ouyang, L. Sun, Z. Zeng, C. Zeng, F. Zeng, S. Wu, *Angew. Chem. Int. Ed.* **2020**, *59*, 10111 – 10121; *Angew. Chem.* **2020**, *132*, 10197 – 10207; b) C. Liu, S. Zhang, J. Li, J. Wei, K. Mullen, M. Yin, *Angew. Chem. Int. Ed.* **2019**, *58*, 1638 – 1642; *Angew. Chem.* **2019**, *131*, 1652 – 1656; c) J. Qi, Y. Fang, R. T. K. Kwok, X. Zhang, X. Hu, J. W. Y. Lam, D. Ding, B. Z. Tang, *ACS Nano* **2017**, *11*, 7177 – 7188; d) Z. Sheng, B. Guo, D. Hu, S. Xu, W. Wu, W. H. Liew, K. Yao, J. Jiang, C. Liu, H. Zheng, B. Liu, *Adv. Mater.* **2018**, *30*, 1800766; e) X. Zhen, J. Zhang, J. Huang, C. Xie, Q. Miao, K. Pu, *Angew. Chem. Int. Ed.* **2018**, *57*, 7804 – 7808; *Angew. Chem.* **2018**, *130*, 7930 – 7934.

[13] a) Y. Ren, A. C. Sedgwick, J. Chen, G. Thiabaud, C. V. Chau, J. An, J. F. Arambula, X. P. He, J. S. Kim, J. L. Sessler, C. Liu, *J. Am. Chem. Soc.* **2020**, *142*, 16156 – 16160; b) D. Xi, M. Xiao, J. Cao, L. Zhao, N. Xu, S. Long, J. Fan, K. Shao, W. Sun, X. Yan, X. Peng, *Adv. Mater.* **2020**, *32*, 1907855; c) L. Teng, G. Song, Y. Liu, X. Han, Z. Li, Y. Wang, S. Huan, X. B. Zhang, W. Tan, *J. Am. Chem. Soc.* **2019**, *141*, 13572 – 13581; d) Z. Hosseinaee, M. Le, K. Bell, P. H. Reza, *Photoacoustics* **2020**, *20*, 100207; e) I. T. Ho, J. L. Sessler, S. S. Gambhir, J. V. Jokerst, *Analyst* **2015**, *140*, 3731 – 3737.

Manuscript received: December 31, 2020
Revised manuscript received: February 4, 2021
Accepted manuscript online: February 10, 2021
Version of record online: March 17, 2021

